Numerical analysis of the deformational behavior of hydrocarbon reservoirs based on an improved elastoplastic constitutive model

O. Roshan[1], E. Taheri[1]*

1- Dept. of Mining, Faculty of Engineering, Tarbiat Modares University, Tehran, Iran

* Corresponding Author: *e_taheri@modares.ac.ir*
(Received: February 2022, Accepted: December 2022)

Keywords

Multiscale

Plastic deformation

Oil reservoir

Porous media

Geomechanical model

Abstract

The goal of the current research is to make more comprehensive the elastoplastic stresses effects and oil reservoirs behave in solid phase. These stresses are largely caused by the behavior of subsurface fluid in reservoirs. In reservoir formations, there are frequently significant spatial changes at various length scales. Additionally, a number of physical events influence the flow model in various hierarchies. To fully describe the flow and deformation concerning all of these sizes, more computing power is required. One of the principal problems in the oil field business has always been how to describe, optimize, and simulate the behavior of the solid portion of oil reservoirs. To model fluid flow in reservoirs, deformable media, and porous media, more effectively, several scales must be taken into account. This approach is difficult in different scales, and the results of the simulation's speed, accuracy, and precision indicates this. A hybrid multi-physical multi-scale model has recently been developed as a solution to this problem. The goal of the current work is to update this model to represent solid-phase deformations better. For this improvement, the model is changed into a geomechanical model with the capacity to simulate a plastic region using an integrated yield function as well as using an implicit technique to solve convergence equations concurrently. The simulation outcomes demonstrate that the improved multi-scale mixed physical model is an effective model for modelling oil reservoirs with elastoplastic deformation. This model's calculation speed and accuracy have been tested, and the results are satisfactory. In addition, this paper modeled land subsidence, which Sokolova et al. claim is impacted by a lack of reservoirs, and it fits quite well with other studies. Results have demonstrated that plastic stresses affect both the rate of oil production and the behavior of subsidence. It can be included as a safety feature for infrastructure and oil surface plants.

1. INTRODUCTION

Increasing the accuracy and precision of oil reservoir modeling is evident due to the growing demand of this market on a global scale. To meet this level of demand, increasing oil extraction rates and production rate must be optimized. Some valuable research was carried out in the field of hydraulic fracturing and simulating of the thermos-hydro mechanical simulation of oil reservoirs [1-3]. However, estimation and calculation of the optimal location of injection wells as well as development of tools and operating method are important issues [4]. In this regard, simulating and modeling the operation of reservoirs play an important role. On the other hand, simulation with high accuracy in a shorter and more efficient time has been one of the constant challenges in this field. Concerning large oil companies, modeling strategy plays a major role in their production strategy [5]. In oil reservoirs modeling, the range of scales varies from millimeters to kilometers, and these scale changes affect the kinetic behavior of the fluid into a reservoir [4]. In order to optimize a simulation, calculating and considering all variables at all scales at the same time does not make sense. Therefore, it seems necessary to invent and develop a method that can maintain valuable information of any scale and process it at the domain of influence. Multi-scale methods for simulating porous oil reservoirs and subsurface layers have been developed to reduce costs and

computational time [6]. In MSFV, the fine scale mass and velocity are balanced. As a result, this method is suitable for modeling fluid behavior and its interaction with the solid phase [7]. The fluid and solid phases are solved in pairs and simultaneously at each time step and a nonlinear loop [8]

In 2019 Skolova et al. worked on Multiscale finite volume method for finite-volume-based simulation of poroelasticity. They proposed a multiscale finite volume method (MSFV) for the simulation of coupled flow-deformation in heterogeneous porous media under elastic deformation (i.e., poroelastic model). They investigated the fine-scale fully resolved system of equations was obtained based on a conservative finite-volume method. In this model, the displacement and pore pressure unknowns were located in a staggered configuration. The coupling was instructed through a coupled formulation. On this coupled finite volume technique, coarse-scale grids for flow and deformation were imposed. They mentioned that local basis positions for scalar pore pressure and vectorial displacement unknowns were then solved over their individual local domains. At the beginning of the simulation, and reused for the rest of the time-dependent simulations. These local basis functions are then clustered to form the prolongation operator. In the proposed multiscale system, finite-volume restriction operators for poroelastic systems were utilized. Once the coarse-scale system was solved, its solution was prolonged back to the original fine-scale resolution, providing the approximate fine-scale solution. The finite-volume multiscale formulation provided conservative stress and mass flux in fine and coarse scale. Several numerical test cases were provided first to validate the fine-scale finite-volume discrete fully-implicit simulation, and then to investigate the accuracy of the proposed multiscale formulation. To recapitulate, the model results are compared with hybrid multiscale Finite Element-Finite Volume (h-MSFE-FV). Our multiscale method enables quantification of the elastic geomechanical behavior via using only a fraction of the fine-scale grid cells, even for highly heterogeneous time-dependent models. As such, it casts a promising approach for field-scale quantification of the mechanical deformation and stress field due to injection and production in a subsurface formation [9].

In 2016 Castelletto et al. worked on multiscale finite-element method for linear elastic geomechanics. They examined the demand for accurate and efficient simulation of geomechanical effects, was widely increasing in the geoscience community. High resolution characterizations of the mechanical properties of subsurface formations were essential to enhance modeling predictions. Such detailed descriptions imposed hard computational challenges and motivate the development of multiscale solution strategies. They proposed a multiscale solution framework for the geomechanical equilibrium problem of heterogeneous porous media based on the finite-element method. After imposing a coarse-scale grid on the given fine-scale problem, the coarse-scale basis functions were obtained by solving local equilibrium problems within coarse elements. Their basis functions form the restriction and prolongation operators used to obtain the coarse-scale system for the displacement-vector. In conclusion, a two-stage preconditioner that couples the multiscale system with a smoother was derived for the iterative solution of the fine-scale linear system. Furthermore, various numerical experiments were presented to demonstrate accuracy and robustness of the method [10].

In 2015 Tene et al. worked on adaptive algebraic multiscale solver for compressible Flow in heterogeneous porous media. They examined the recently developed AMS for incompressible (linear) flows [Wang et al., JCP, 2014], C-AMS operates by defining primal and dual-coarse blocks on top of the fine-scale grid. Furthermore, they mentioned that these coarse grids facilitate the construction of a conservative (finite volume) coarse-scale system and the computation of local basis functions, respectively. Therefore, several basis function formulations (incompressible and compressible, with and without accumulation) are considered to construct an efficient multiscale prolongation operator. As for the restriction operator, C-AMS allows for both multiscale finite volume (MSFV) and finite element (MSFE) methods. Finally, to resolve high-frequency errors, fine-scale (pre-and-post) smoother stages are employed. They examine different factors for reducing computational expense, and they found that the C-AMS operators (prolongation, restriction, and smoothers) are updated adaptively. In this regard, they indicated that an efficient C-AMS strategy for heterogeneous 3D compressible problems is developed based on overall CPU times. In conclusion, C-AMS is compared against an industrial-grade Algebraic Multigrid (AMG) solver. The results of this comparison illustrate that the C-AMS is quite efficient as a nonlinear solver, and precise when iterated to machine accuracy [11].

In 2015 Cusini et al. examined the constrained pressure residual multiscale (CPR-MS) method for

fully implicit simulation of multiphase flow in porous media. They investigated the first multiscale method for fully implicit (FIM) simulations of multiphase flow in porous media, namely CPR-MS method. In their article built on the FIM Jacobian matrix, the pressure system was obtained by employing a constrained pressure residual (CPR) operator. Multiscale finite element (MSFE) and finite volume (MSFV) methods were then formulated algebraically to obtain efficient and accurate solutions to their pressure equation. They consider the multiscale prediction stage (first-stage) was coupled with a corrector stage (second-stage) employed on the full system residual. The converged solution was enhanced through outer GMRES iterations preconditioned by these first and second-stage operators. While the second-stage FIM stage was solved using a classical iterative solver, the multiscale stage was investigated in full detail. They concluded that several choices for fine-scale pre-and post-smoothing along with different choices of coarse-scale solvers are considered for a range of heterogeneous three-dimensional cases with capillarity and three-phase systems. Finally, they mentioned that the CPR-MS method is the first of its kind and extends the applicability of the so-far-developed multiscale methods (both MSFE and MSFV) to displacements with strong coupling terms [12].

In 2014 Hajibeigi and his coworker worked on compositional multiscale finite-volume formulation. They investigated a sequential-implicit strategy was used to deal with the coupling of the flow (pressure) and transport (component overall concentration) problems. In their article compositional formulation, the overall continuity equation was used to formulate the pressure equation. The resulting pressure equation conserves total mass by construction and depends weakly on the distributions of the phase compositions. The transport equations were expressed in terms of the overall composition; hence, phase-appearance and -disappearance effects do not appear explicitly in these expressions. Details of the MSFV strategy for the pressure equation were described in their article. The only source of error in this MSFV framework is the localization assumption. No additional assumptions related to complex physics were used. To recapitulate, for ID problems, the sequential strategy was validated against solutions obtained by a fully implicit simulator. The accuracy of the MSFV method for compositional simulations was then illustrated for different test cases [13].

In 2016 Wang et al. investigated monotone multiscale finite volume method. They investigated the causes of the non-monotone solutions which were identified and connected to the local flux across the boundaries of primal coarse cells induced by the basis functions. They proposed a monotone MSFV (m-MSFV) method based on a local stencil-fix that guarantees monotonicity of the coarse-scale operator. Detection of non-physical transmissibility coefficients that lead to non-monotone solutions was achieved only by using local information and aimed to perform algebraically. For investigating the 'critical' primal coarse-grid interfaces, a monotone local flux approximation, specifically, a Two-Point Flux Approximation (TPFA), was employed. For practical applications, an adaptive approach based on normalized positive off-diagonal coarse scale transmissibility coefficients was developed by them. Based on the histogram of these normalized coefficients, they can remove the large peaks by applying the proposed modifications only for a small fraction of the primal coarse grids. Finally, the m-MSFV approach can guarantee monotonicity of the solutions to any desired level. Numerical results illustrate that employing the m-MSFV modifications only for a small fraction of the domain can significantly reduce the nonmonotonicity of the conservative MSFV solutions [14].

In 2015, Taheri et al. presented a multi-scale multi-physical hybrid model M^{3}GM (Mixed Multiscale Multiphysics Geomechanical Model), which is also the main basis of the present study [15]. In the mentioned model, the solid phase deformations are calculated by elastic equations. Then the effect of surrounding rocks on the deformation of the reservoir is considered [16]. In geotechnical studies, applying a comprehensive hydraulic and mechanical model for saturated and semi-saturated rocks and soils has always been discussed. The saturation degree effect and volumetric strain on the mechanical and hydraulic behavior of the characteristic model has always been important. In this regard, in order to model M^{3}GM, which is the basis of the present study, a unified model has been used to simulate the solid phase more accurately. This model in 2018 is as CASM model or unified bounding surface model which Moghadam et al. in order to improve the problems caused by explicit integration method in the models, using the implicit integration method to model the behavior of clay and sand to simulate sand liquefaction presented. Moreover, utilizing constitutive models for coupling of hydraulic and mechanical behaviors of unsaturated soils and rocks is an interesting subject in geotechnical studies. In this regard, the plastic framework was

developed by Moghadam and his colleagues for considering elastic and plastic deformation in an implicit approach [17]. The results obtained from the CASM model aforementioned that this model showed a good performance in compare to previous model.

In 2015 Nikadat et al. presented a numerical modelling of stress analysis around rectangular tunnels with large discontinuities (fault) by a hybridized indirect BEM. They investigated the effect of large discontinuities (fault) behavior on a jointed medium around the rectangular tunnel. The stress distribution around the tunnels dug in jointed rock masses was investigated using a hybridized indirect boundary element algorithm called TFSDDM (fictitious stress displacement discontinuity technique). For a more precise analysis of discontinuity effects, their code combined the benefits of the fake stress and displacement discontinuity approaches. Their findings demonstrate that the stress distribution around the tunnel was significantly impacted by the dip angle of discontinuities. Additionally, it was demonstrated that increasing the discontinuities dip angle in the roof will provide a reduction in the roof's tensile stress. In the roof, stresses reached 8 MPa, but because of the dilatation effect, they increased to 13 MPa [18].

Also, its finite element program in soil and rock environments has shown good results due to the stress space q-p'. This model was proposed based on the concept of bounding surface and using the implicit method. For this purpose, it was applied as a base model in the upgraded model of multi-scale multi-physical plastic in the solid phase. In order to establish the interaction of fluid and solid in an oil reservoir, several series of coupling equations must be solved simultaneously. So, obtaining a proper rate in all sectors, demand for a proper prototype and its compatibility with the base model is undeniable. Hence, the use of the implicit method (skin) and Newton-Raphson modified rings in the new model has greatly contributed to this framework. Furthermore, due to the integration of the submission function under the shapeable program and the new formulation, it is possible to have a better simulation of the solid phase in oil reservoirs. The unified plastic constitutive model uses the radial mapping role and simulation of smooth behavior to predict and model the interaction with fluid phases in the base model. The base model also uses the law of isotropic hardening for the solid phase.

2. MODEL INTRODUCTION

In this section, an enhanced mixed multi-scale multi-physics geomechanical model (EM^{3}GM) is introduced. First, the governing equations examination for presenting the multi-scale method of finite volumes and the model mechanism is introduced, then the plastic model in rock is introduced. Finally, the interaction of the fluid and solid phases and the coexistence of both models to obtain a unified scheme are expressed. The third section also provides examples for model validation.

2.1. The governing equations and the EM^{3}GM model

The inclusive phase system in this model consists of a combination of a deformable porous media as the solid phase and water, gas and oil as the fluid phase. The solid phase is examined from the Lagrangian point of view and the fluid phase from the Eulerian point of view. It is important to note that the fluid phase and the solid phase behave separately in the context of multidimensional models of finite volumes and finite components.

The inclusive phase system in this model consists of a combination of a deformable porous media as the solid phase and water, gas and oil as the fluid phase. The solid phase is examined from the Lagrangian point of view and the fluid phase from the Eulerian point of view. It is important to note that the fluid phase and the solid phase behave separately in the context of multidimensional models of finite volumes and finite components.

$$\frac{D}{Dt}(\phi S_\alpha \rho_\alpha) + \phi S_\alpha \rho_\alpha \nabla v_\alpha = \dot{m}_\alpha \qquad (1)$$

In the above equation φ porosity is ρ_α phase density and S_α is the degree of phase saturation and v_α is the phase velocity. Also, $\dot{m}_\alpha$ stands for wells and source terms. In the following, according to the definition of relative velocity, which is $W = v_\alpha - v_s$, and with a little mathematical work:

$$\frac{D^s}{Dt}(\phi S_\alpha \rho_\alpha) + \nabla(\phi S_\alpha \rho_\alpha w_\alpha) + \phi S_\alpha \rho_\alpha \nabla v_s = \dot{m}_\alpha \qquad (2)$$

After summation of the phases, we will have:

$$\phi\frac{D^s}{Dt}\sum_{\alpha=1}^{n_p}S_\alpha\rho_\alpha+\sum_{\alpha=1}^{n_p}S_\alpha\rho_\alpha\frac{D^s\phi}{Dt}+\sum_{\alpha=1}^{n_p}\nabla(\phi S_\alpha\rho_\alpha w_\alpha)+\sum_{\alpha=1}^{n_p}\phi S_\alpha\rho_\alpha\nabla v_s=\dot{m}_\alpha \quad (3)$$

Equation 3 is the general equation of fluid motion in a porous media. However, to obtain the interaction behavior of each phase, the momentum equation of equilibrium of each phase must also be considered.

To investigate the momentum equilibrium for fluid phases, several assumptions are considered:

- Fluid flow follows Darcy's law
- Small solid phase velocity and acceleration are ignored
- Solid particles are incompressible

The linear equation of the momentum equilibrium of the fluid phases is as follows:

$$\phi S_\alpha w_\alpha=\lambda_\alpha.(-\nabla p+\rho_\alpha g) \quad (4)$$

In the above equation λ_α is the phase mobility tensor which is defined as the equation $\lambda_\alpha=\frac{Kkr_\alpha}{\mu_\alpha}$. In this equation K is the absolute permeability tensor, kr_α is the relative permeability and μ_α is the viscosity of each phase. Placing Equation 4 in Equation 3 and considering the phase mobility capability we will have:

$$\phi\frac{D^s}{Dt}\sum_{\alpha=1}^{n_p}S_\alpha\rho_\alpha+\sum_{\alpha=1}^{n_p}S_\alpha\rho_\alpha\frac{D^s\phi}{Dt}+\sum_{\alpha=1}^{n_p}\nabla.(\rho_\alpha\frac{Kkr_\alpha}{\mu_\alpha}.(-\nabla p+\rho_\alpha g))+\sum_{\alpha=1}^{n_p}\phi S_\alpha\rho_\alpha\nabla v_s=\dot{m}_\alpha \quad (5)$$

The solid phase equilibrium equation is transformed as follows:

$$\nabla.\sigma+\rho g=0 \quad (6)$$

It is important to note that in the rock mechanics, effective stress is generally considered, so we will have an effective stress equation:

$$\sigma'=\sigma-Ip \quad (7)$$

In the above equation, p is the fluid pressure. Considering the relationship between strain and deformation and defining volumetric strain and solid phase velocity, we have:

$$\phi\frac{D^s}{Dt}\sum_{\alpha=1}^{n_p}S_\alpha\rho_\alpha+\sum_{\alpha=1}^{n_p}S_\alpha\rho_\alpha\frac{D^s\phi}{Dt}+\sum_{\alpha=1}^{n_p}\nabla.(\rho_\alpha\frac{Kkr_\alpha}{\mu_\alpha}.(-\nabla p+\rho_\alpha g))+\sum_{\alpha=1}^{n_p}\phi S_\alpha\rho_\alpha\frac{\varepsilon_{vol}}{\Delta t}=\dot{m}_\alpha \quad (8)$$

Also, the degree of phase saturation is considered as Equation 9.

$$\sum_{\alpha=1}^{n_P}S_\alpha=1 \quad (9)$$

After introducing the original phase equations, the equations of the enhanced mixed multi-scale multi-physics model are expressed: After discretizing Equation 8, we have:

$$\phi_\alpha^{n+1}\frac{\rho_\alpha^{n+1}S_\alpha^{n+1}-\rho_\alpha^nS_\alpha^n}{\Delta t}+\rho_\alpha^nS_\alpha^n\frac{\phi^{n+1}-\phi^n}{\Delta t}$$
$$-\nabla.(\rho_\alpha^{n+1}\lambda_\alpha(\nabla p^{n+1}-\rho_\alpha^{n+1}g\nabla z)+\phi_\alpha^{n+1}\rho_\alpha^{n+1}S_\alpha^{n+1} \quad (10)$$
$$\frac{\varepsilon_v^{n+1}-\varepsilon_v^n}{\Delta t}=\rho_\alpha^{n+1}q_\alpha$$

After separating the phase density and to obtain the pressure equation and after the summation of the phases, we will have:

$$\frac{\phi^{n+1}}{\Delta t}+\frac{-\phi^n}{\Delta t}\sum_{\alpha=1}^{n_p}B_\alpha^{n+1}\rho_\alpha^nS_\alpha^n-\sum_{\alpha=1}^{n_p}B_\alpha^{n+1}\nabla(\rho_\alpha^{n+1}\lambda_\alpha$$
$$(\nabla p^{n+1}-\rho_\alpha^{n+1}g\nabla z))+\phi^{n+1}\frac{\varepsilon_v^{n+1}-\varepsilon_v^n}{\Delta t}=q_t$$
$$q_t=\sum_{\alpha=1}^{n_p}q_\alpha$$
$$B_\alpha$$
$$\nu+1$$
$$C_c$$
$$(\Omega k\in[1,M])$$
$$(\Omega^h\in[1,N])$$
$$\varphi_k^h \quad (11)$$
$$\varphi^h$$
$$\partial\Omega_k$$

Where $q_t=\sum_{\alpha=1}^{n_p}q_\alpha$ is the flow rate and B_α is the volumetric factor (phase density inverse). The linearization of the above equation results in an iterative pressure equation.

$$C_c(p^{\nu+1}-p^\nu)-\sum_{\alpha=1}^{n_p}B_\alpha^\nu\nabla.(\rho_\alpha^\nu\lambda_\alpha\nabla p^{\nu+1})=\frac{-\phi^\nu}{\Delta t}+\frac{\phi^n}{\Delta t}$$
$$\sum_{\alpha=1}^{n_p}B_\alpha^{n+1}\rho_\alpha^nS_\alpha^n+q_t-\sum_{\alpha=1}^{n_p}B_\alpha^\nu\nabla.(\rho_\alpha^{\nu^2}\lambda_\alpha g\nabla z)-\phi^\nu\frac{\varepsilon_v^\nu-\varepsilon_v^n}{\Delta t} \quad (12)$$

The new and old iteration steps are denoted by $\nu+1$ and ν. In the following:

$$C_c=-\phi^\nu\sum_{\alpha=1}^{n_p}\frac{\partial B_\alpha}{\partial p}\Big|\rho_\alpha^nS_\alpha^n \quad (13)$$

In Equation 13 C_c is the coefficient of compressibility. In the following term, convection as:

$$\sum_{\alpha=1}^{n_p} B_\alpha^\nu \nabla.(\rho_\alpha^\nu \lambda_\alpha \nabla p^{\nu+1}) \approx \nabla.(\lambda_t.\nabla p^{\nu+1}) - \nabla(\lambda_t.\nabla p^\nu) + \sum_{\alpha=1}^{n_p} B_\alpha^\nu \nabla.(\rho_\alpha^\nu \lambda_\alpha \nabla p^\nu) \quad (14)$$

By placing Equation 14 in Equation 12 we will have:

$$\frac{C_c}{\Delta t}(p^{\nu+1} - p^\nu) - \nabla.(\lambda_t.\nabla p^{\nu+1}) = RHS^\nu \quad (15)$$

Which in Equation 15:

$$\sum_{\alpha=1}^{n_p} B_\alpha^\nu \nabla.(\rho_\alpha^{\nu^2} \lambda_\alpha g \nabla z) - \phi^\nu \frac{\varepsilon_\nu^\nu - \varepsilon_\nu^n}{\Delta t} - \nabla(\lambda_t.\nabla p^\nu) + \sum_{\alpha=1}^{n_p} B_\alpha^\nu \nabla.(\rho_\alpha^\nu \lambda_\alpha \nabla p^\nu) \quad (16)$$

The structure of the multi-scale finite volume method is based on two categories of networking called large networking (Figure 1 on the right) and auxiliary networking (Figure 1 on the left). The large network consists of M large cells ($\Omega_k \in [1, M]$) and the auxiliary network consists of N helper cells ($\Omega^h \in [1, N]$).

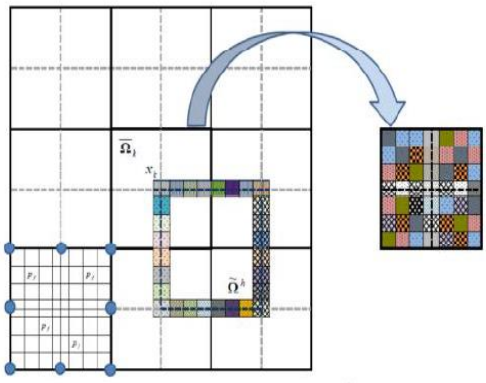

Fig. 1. Displays large cells, helper cells, and internal microgrids, as well as helper cell boundaries. The eight-node element is displayed on the left.

The MSFV structure has two main operators. The first uses the integration of microscale pressures obtained from two series of basic and correction functions φ_k^h and φ^h , to increase the permeability effect to a higher scale. The second operator uses the above functions to obtain a stable microscale pressure. Unlike classical methods, these operators are not analytic functions, but are derived from the public and private solution of Equation 15. More precisely, the basic and corrective functions of the public and private solutions of Equation 15 are reduced by considering the boundary conditions.

$$(\tilde{n}^h.\nabla)((\lambda_t.\nabla \phi_k^h) = 0 \quad (17)$$

$$(\tilde{n}^h.\nabla)((\lambda_t.\nabla \partial \phi^h).\tilde{n}^h) = RHS^\nu \quad (18)$$

In the above equations, $\tilde{n}^h$ is the normal vector out of the $\partial \emptyset^h$ boundary. The boundary conditions at the nodes of the center of the auxiliary network are x_1 as $\emptyset^h(x_1) = 0$ and $\emptyset_k^h(x_1) = \delta_{kl}$. It is worth noting that the magnitude of physical phenomena such as capillaries, mass exchange between phases in RHS equation 18 is seen with the distribution of correction functions. By overlapping two sets of functions, the microscale pressure is obtained as follows.

$$p_f(x) \approx p'(x) = \sum_{h=1}^{N}(\sum_{k=1}^{M}(\phi_k^h(x)\tilde{p}_k + \phi^h(x)) \quad (19)$$

In the above equation $\tilde{p}_k$ the pressure at the center of the nodes of each large cell is x_k . By placing equation 19 in equation 15 and integrating it into large cells and applying Gauss's law, we have:

$$\int_{\bar{\Omega}l} \frac{C_c}{\Delta t}(\sum_{h=1}^{N}(\sum_{k=1}^{M}(\phi_k^h \tilde{p}_k^{\nu+1} + \phi^{h^\nu}) - p'^\nu) d\Omega - \int_{\partial\bar{\Omega}}(\lambda_t.\sum_{h=1}^{N}(\sum_{k=1}^{M}(\phi_k^h \tilde{p}_k^{\nu+1} + \phi^{h^\nu})).\tilde{n}_l d\Gamma = \int_{\bar{\Omega}l} RHS^\nu \quad (20)$$

The result of the above equation is a repeating nonlinear equation system.

$$A_{lk} p_k^{\nu+1} = b_l^\nu \quad (21)$$

$$A_{lk} = \sum_{h=1}^{N}(\int_{\bar{\Omega}} \frac{C_c}{\Delta t}\phi_k^h d\Omega - \int_{\partial\bar{\Omega}L}(\lambda_t.\nabla\phi_k^h + \tilde{n}_l d\Gamma) \quad (22)$$

$$b_l^\nu = \int_{\bar{\Omega}}(RHS^\nu + \frac{C_c}{\Delta t}p'^\nu) d\Omega - \sum_{h=1}^{N}(\int_{\bar{\Omega}} \frac{C_c}{\Delta t}\phi^{h^\nu} d\Omega) - \int_{\partial\bar{\Omega}} \lambda_t.\nabla\phi^{h^\nu}.\tilde{n}_l d\Gamma) \quad (23)$$

The iteration process continues until it reaches the convergence limit. $\left\| p'^{\nu+1} - p'^\nu \right\| < \beta$.

The resulting pressure field is not constant, a condition that is necessary to solve the transfer equation. As a result, another step is needed to stabilize the pressure field. It has already been stated that the pressure field is applied to obtain a microscale flux in each large cell. Equation 15 is solved by the Newman boundary condition at the microscale pressure.

$$-\nabla.(\lambda_t.\nabla p'') = RHS^{\nu} \quad (24)$$

With, $-\lambda_t.\nabla p^{''}$ in $\partial\Omega_k$. The new pressure field p'' is constant and can be used to solve the mass equation (Equation 3).

2.2. Solid phase discretization and FE structure

In order to discretize the solid phase momentum equation, the Galerkin method is used regardless of the volumetric forces:

$$\int_{\Omega} W_u^t (L^T\sigma - \rho g)d\Omega + \int_{\Gamma u} \bar{W}_u^t (L^T\sigma - \bar{t})d\Gamma = 0 \quad (25)$$

In the above equation, W_u^t and $\bar{W}_u^t$ are weight functions on boundaries. L is the skeletal tangent constant and $\bar{t}$ is the amount of external force on the boundaries of the environment

Applying the Gaussian law where $B = LN_u$ we have:

$$\int_{\Omega} B^T \sigma d\Omega = \int_{\Gamma^N} N_u^T \bar{t} d\Gamma \quad (26)$$

Which in the above equation N_u is a function of shape. By applying the strain stress relationships of the equation as:

$$\int_{\Omega} B^T (D\varepsilon)d\Omega = \int_{\Gamma^N} N_u^T \bar{t} d\Gamma - \int_{\Omega} B^T (pm)d\Omega \quad (27)$$

In the above equation, D is a plastic matrix. In the following, by using the relations of stress and displacement and using the functions of shape, we will have the relation $B=LN_u$:

$$(\int_{\Omega} B^T (DB)d\Omega)\hat{u} = -\int_{\Gamma^N} N_u^T \bar{t} d\Gamma + \int_{\Omega} B^T (pm)d\Omega \quad (28)$$

The device creates the following equation to move the nodes u.

$$K\hat{u} = F \quad (29)$$

$$K = \int_{\Omega} B^T (DB)d\Omega)\hat{u} \quad (30)$$

$$F = -\int_{\Gamma^N} N_u^T \bar{t} d\Gamma + \int_{\Omega} B^T (pm)d\Omega \quad (31)$$

The second part of the right-hand side of the equation, called F_2 , is obtained by integrating all the tiny cells into one large cell.

$$F_2 = \sum_{i=1}^{i=nfs} B_i^T P_i .m.A \quad (28)$$

In the above relation P_i is the microscale pressure and A is the sectional area of each cell.

2.3. Plastic response

General formulation of the model is 3D stress space in the rock. According to the definitions of effective stress formulas, the mean and deviatoric are represented by P' and q, respectively. Finally, it is assumed that the strain has been decomposed, it is from 2 parts elastic and plastic. After stating the definitions of the general parameters, the critical state of the rock must be defined. This condition occurs in the rock when the stress and dilation ratio reach zero and the shear strain occurs. In the present model, this state is shown as a line in the $e - ln\,p^{'}$ space. In the following equations are expressed:

$$e_{cr} = e_{\Gamma} - \lambda_{cr} \ln p' \quad (33)$$

$$q = M_{cr} p' \quad (34)$$

In order to introduce the elastic behavior of the model, volumetric and shear modulus are defined:

$$K = \frac{\nu p'}{k} \quad (35)$$

$$G = \frac{3(1-2\mu)}{2(1+\mu)} K \quad (36)$$

In the mentioned relations $\nu = 1 + e$ specific volume, K shows the slope of the loading-unloading line in the plane $\nu - ln\,p^{'}$ and μ represents the Poisson's ratio.

It was also mentioned in the original model that the solid phase in finite elements comprises part of the elastic matrix. But the plastic behavior of the model is not affiliated with the classical models. Because in classical models, the inner region of the yield surface is completely elastic [19]. This assumption depicts that in such models the behavior of the rock does not exceed the elastic state until the yield value is reached. When the rock reaches the yield surface, it then simulates the plastic behavior. This means predicting elasticity to the yield surface and then the behavior of the plastic, causing an abrupt behavior from elastic to plastic in the rock. However, laboratory observations show that the behavior in rocks in transition from elastic to plastic is gradual.

In the present model, in order to eliminate this defect and to predict more accurately, plus, simulating the behavior of the rock in transition from elastic to plastic, the concept of the surrounding surface and sub-loading surface have been used. The concept of bounding surface was first proposed by Dafalias and Popov and the sub-loading surface examined by Hashiguchi [20].

This is the case in the bounding surface theory, and it is assumed that the deformation of the plastic begins from the very beginning of the load. It is further assumed that the elastic part decreases to a point [20]. Two levels, internal and external, are used to describe this type of behavior. Description of these two hypothetical surfaces is that the inner surface is considered as the loading surface and it is assumed that the stress point definitely passes through this surface. The bounding surface in this theory is the same as the external level. The image of the stress state is placed on this surface.

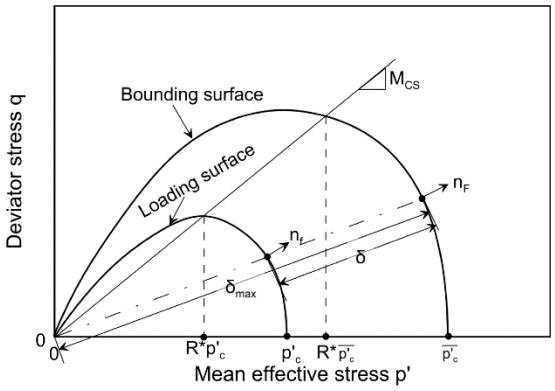

Fig. 2. Loading surface, bounding surface and radial mapping law, according to the bounding surface theory [21].

However, the law of radial mapping has been used to explain how the state of stress is depicted on the bounding surface. Accordingly, the stress point of the image on the bounding surface is determined by the straight line passing through the origin of the stress space and the current stress point on the loading surface, the image stress on the bounding surface [19].

Due to the geometric similarity of the loading and bounding surface, the following relation is established for the stress components:

$$\gamma = \frac{\sigma}{\sigma_j} = \frac{q}{q_j} = \frac{p'}{p'_j} = \frac{p'_c}{p'_{cj}} \qquad (37)$$

In this equation, μ is defined as the ratio of the size of the surfaces and the amount of distance of the loading surface to the bounding surface. In the above relation, σ characterizes the current stress state, P' indicates the mean effective stress component and q is the differential stress component corresponds to the current stress state. In addition, σ_j represents the image stress state on the bounding surface, p'_j represents the mean effective stress component, and q_j represents the differential stress component corresponding to the image stress state. Also, p'_c controls the size of the loading surface and p'_g is the isotropic hardening parameter and determines the size of the bounding surface [19].

After expressing the bounding level, it is time to load the surface. To describe this level in rocks, the U-yield function in the model is used.

This function is defined according to the following relation:

$$F(\sigma) = (\frac{q}{M_{cr} p'})^N + \ln(\frac{p'}{p'_c}) / \ln(R) \qquad (38)$$

Where N and R are the parameters of the material. The N controls the shape of the loading surface, and the R expresses the ratio between the values of P' and p'_c at the point of collision of the yield surface and the line of the critical state.

Also, the bounding surface function as:

$$F(\sigma_J) = (\frac{q_j}{M_{cr} p'_j})^N + \ln(\frac{p'_j}{p'_{cj}}) / \ln(R) \qquad (39)$$

To explain the stress and strain behavior of rocks, especially petroleum reservoir rocks, which are generally carbonate or clayey and sandy, it is essential to establish a relationship between the plastic volumetric strain rate and the plastic differential strain rate. This connection is called the law of dilation [21].

According to this law, in modeling the behavior of clay and sand, the relationship must describe well the behavior of these two types of rocks during loading.

The law of general dilatancy rule is obtained according to the following equation [22]:

$$d = \frac{d\varepsilon_v^p}{d\varepsilon_q^p} = \frac{d_0}{M_{cr}}(M_{cr} e^{\beta\psi} - \eta) \qquad (40)$$

In the above equation d represents dilation, $d\varepsilon_v^p$ increases the plastic volumetric strain, $d\varepsilon_q^p$ increases the plastic differential strain, d_0 and β the parameters of material and η determine the stress ratio.

To better show the plastic behavior of the rock, in the proposed model, the direction of the plastic strain vector is determined by the vector perpendicular to the surface of the plastic potential. This function, known as the plastic potential function, is obtained by integrating the following equation:

$$Q(\sigma) = \frac{q}{p'} + \frac{d_0 e^{\beta\psi}}{1 - \frac{d_0}{M_{cr}}}(1 - (\frac{p'_0}{p'})^{1 - \frac{d_0}{M_{cr}}}) \qquad (41)$$

Where p'_0 determines the size of the plastic potential surface.

But an important part in the plastic model used in the advanced model is the incoherent flow law in modeling the plastic deformations. According to the definition of this law, which states that the direction of the plastic strain vector is in the same direction as the vector perpendicular to the plastic potential surface, the following relationship is considered:

$$d\varepsilon^p = \frac{d\lambda \frac{\partial Q}{\partial \sigma}}{\left\| \frac{\partial Q}{\partial \sigma} \right\|} = d\lambda . m \quad (42)$$

Where $m = \frac{d\lambda \frac{\partial Q}{\partial \sigma}}{\left\| \frac{\partial Q}{\partial \sigma} \right\|}$ specifies the unit vector perpendicular to the plastic potential surface and the direction of the plastic strain vector is determined by this vector. $d\lambda$ is the plastic coefficient [21]. Also, the rate of increase in plastic strain of volumetric and differential components is obtained using the following equations:

$$d\varepsilon_v^{\ p} = \frac{d\lambda \frac{\partial Q}{\partial p'}}{\left\| \frac{\partial Q}{\partial \sigma} \right\|} = d\lambda . m_p \quad (43)$$

$$d\varepsilon_q^{\ p} = \frac{d\lambda \frac{\partial Q}{\partial q}}{\left\| \frac{\partial Q}{\partial \sigma} \right\|} = d\lambda . m_q \quad (44)$$

2.4. Determining the elastic state or plastic

In the continuation of the modeling process and when the deformation is entered into the model, it is time to model the loading space and determine the type of deformation of the rock based on the amount of stress. At this time, in each loading step, the stress state is calculated as follows, assuming that the strains are elastic:

$$\sigma^{Trial} = \sigma_n + D^e{}_{n+1} d\varepsilon_{n+1} \quad (45)$$

In this equation, σ^{Trial} specifies the elastic state stress, *n* and *n+1* represent the previous step and the current step, and D^e represents the material elastic parameter matrix. During this process, the behavior of material assumed elastic and the other state variables remain constant and equal to their previous state. In the continuation of the process, the amount of elastic stress state and other variables are corrected in the plastic correction process [19].

But when the stresses exceed, a plastic correction process occurs. At this time, the amount of elastic stress specified in the previous process, the law of flow, the law of stiffness and the changes in the size of the surfaces are corrected in the way of implementing the compatibility conditions.

The following equations will be involved in this process.

Equilibrium equation:

The necessary condition in this equation is always the state of stress. This means that the amount of stress must implement the balance.

$$d\sigma = D^e d\varepsilon^e \quad (46)$$

By integrating in different steps from the above equation and placing it in equation (45), the following equation is obtained:

$$\sigma_{n+1} = \sigma^{Trial} - D^e{}_{n+1} d\varepsilon^p{}_{n+1} \quad (47)$$

To form the plastic strains, the following relation must be established:

$$,\left\| d\gamma = U(\gamma) \right\| d\varepsilon^p \left\| 0 d\varepsilon^p \right\| \neq 0 \quad (48)$$

So, by implicit integral numericalization of this equation we have:

$$\gamma_{n+1} = \gamma_n - u \ln(\gamma_{n+1}) d\lambda \quad (49)$$

After that and by satisfying the compatibility conditions and the law of isotropic hardening, the system of nonlinear equations is formed, which Newton-Raphson iteration method is used to solve. After solving the output of the elastic model, it is returned to the model in the form of force to be compared with the amount of stress resulting from the solution of the mass equation and returned to the equilibrium equation and these two series of equations converge.

2.5. The interaction of fluid and solid phases

In previous sections, it is stated that there are two main solutions to solve the issue of interaction. One explicit solution and the other two-sided iterative solution. For the base model as well as the elastic model of the plastic used to upgrade the base model, the repeated two-way solution method has been used. This method is used to create and solve the interaction between the structure of the multidimensional finite volume method for the fluid phase as well as the finite element method that models the solid phase.

To do this, the system of fluid and solid equations are connected to a Newton-Raphson iteration loop. For the input of the finite element method, constant multiscale pressure is used to obtain the deformations, which are applied in the finite element cell space. The number of degrees of freedom of the constituent cells is 2. But as mentioned, the method used for the interaction is repetitive. As a result, for the convergence of the equations, the calculated pressure must be returned to the calculation cycle for convergence to occur. The method of operation is such that at the beginning and after each time step in the first stage, the phase mobility is checked. It should be noted that this feature is affected by changes in saturation. After checking this value and if the phase mobility is more than its allowable limit, the basic functions are recalculated and updated. If the phase mobility is within the allowable range, the problem enters the entanglement loop of the other two phases, i.e., liquid and solid. This loop is where the pressure correction function is calculated and the pressure-dependent values are updated. As a result, these functions are updated based on pressure. After this operation and extraction of the main functions from the relations (17) and (18) of the system of equations are formed and the matrix of coefficients and vectors to the right of the equation is formed. To solve the problem, large-scale pressures are extracted and then using equation (19) the microscale pressures are obtained. At this stage, a limitation is considered to check that the microscale pressure is not exceeded in two consecutive steps. If this difference does not exceed the set limit, the pressure equation is solved based on microscale pressures. But this is where the elasto-plastic model comes into play. In this way, the output of the equation is the mass of pressure, as stated, after passing the mentioned conditions, it enters the equation of equilibrium and outputs the deformations. The output of the equilibrium equation is the phase deformation of the solid zone. In the basic model, this deformation was returned to the mass equation to converge. But at this stage, the output deformation of the equilibrium equation enters the elastic model. It should be noted that at this stage the output deformations of this equation are elastic and strain stress calculations have not yet been performed on them. Also, the plastic strain system and the model are used. It is a control strain model and uses the strain input to perform calculations. The output deformation of the equilibrium equation enters the elastic program and the program gives it as output stress. In this step, it is determined whether, with the calculated stress, the deformation remains in the elastic range or enters the plastic-elastic or even plastic stage. Under the elasto-plastic program, it is first determined whether the input of the given model has been drained or not. It then calculates the output stress using the potential and new and integrated yield function. For convergence, as mentioned, the Newton-Raphson ring is also used in this program. It should also be noted that this program also uses the concept of effective tension. Using the condition of the yield function and checking the yield level, whether or not to cross the elastic range, the system of equations is formed and solved by the two-way iterative method and the Newton-Raphson loop. The output voltage is also converted to force and is the output of the program. It should be noted that the structure of the program performance is such that the initial calculations in the base program are based on the elastic state. The output of these calculations as the input of the elastic model creates an unbalanced force.

In this step, the difference of the obtained force is obtained from the elastic force calculated by solving the mass equation. Newton Raphson is also used in this stage. This force difference, as the right-hand side of the force, refers to the equilibrium equation. But the point is that this force is no longer based on elasticity and may be elastic in the plastic or the plastic range. After the force is returned to the equilibrium equation and the iterative solution is solved, the output of the equilibrium equation, which was the deformation and subsequent volumetric strains, is obtained based on the new applied force. The resulting deformations and strains are then returned to the mass equation and the cycle is repeated. It should be noted that Newton Raphson was also used at this stage. In other words, the three sets of equations must be cross-sectionally converged with each other. Following the continuation of this process, the deformations are obtained based on the elasticity of the plastic or plastic, and the interaction of the liquid and solid phases is completed. After convergence of the obtained pressures, the flux due to the resulting pressure is applied to the boundaries of each sub-zone, and a stable pressure is obtained. This step is necessary for mass stability to solve the transfer equation. Finally, after extracting the constant pressures, the degree of saturation of the fluid phases is determined. And the degree of saturation equation is solved. In addition to the above, physical properties such as porosity are constantly updated. In this regard, using the solid phase mass survival equation:

$$\phi = (1-(1-\phi_0)\exp-\varepsilon_{vol}) \quad (50)$$

Table 1. Model algorithm, main time steps and iteration loop

EM3GM Pseudo Code
Start simulation n = 1 do loop I: time step $\boldsymbol{v_c = 1, p^{v_c} = p^n}$ do loop II: Newton coupler repeating loop $\boldsymbol{v_p = 1 : p^{v_p} = p^{v_c}}$ do loop III: repeat for pressure Update correction functions Solve the linearized equation of pressure $\boldsymbol{\Rightarrow p^{v_{p+1}}}$ $\boldsymbol{v_p = v_p + 1}$ until (Convergence of the nonlinear pressure equation) CASM Model Investigation of elastic or plastic stresses Solve the system of nonlinear equations Volumetric strain calculation and porosity update Updating stress and pressure in equation $\boldsymbol{p^{v_{c+1}} = p^{v_p}}$ until (Convergence of pressure equations and geomechanics) a constant flux applied Solve the transfer equation $\boldsymbol{S_\alpha^{n+1} = S_\alpha^n}$ (end of the simulation) until

3. PLAIN STRAIN SUBSIDENCE

Geoengineering applications have a real challenge in modeling land subsidence caused by shortage of reservoirs. For the sake of this numerical experiment, we assume that the subsurface is a heterogeneous porous media with varying elastic effects along the z-axis. This hypothesis shows that given plane strain, circumstances a 3D issue may be reduced to a 2D problem. The dynamics of fluid flow inside the reservoir are not simulated since the focus of this work is on simulating the mechanical deformation in response to total reservoir depletion. This study is based on the Sokolova et al. article which they published in 2019 [6].

The producing reservoir is 1000 meters deep, 1200 meters wide, and 120 meters thick. Within a 10 km radius, mechanical deformation is modeled at distances of 3 km in both the y and x directions. Assuming a normal fluid angle of 0.1 bar/m, an initial reservoir pressure of 100 bar corresponds to a properly pressured formation at the depth under discussion. The distribution of young's modulus in the subsurface for one-dimensional vertical compressibility, manifested in the northern Adriatic sedimentary basin, is determined using a constitutive model. In this approach, the total vertical stress y' and hydrostatic pressure are superimposed to give the vertical effective stress, which is then estimated as the vertical uniaxial compressibility CM. The Poisson ratio ν=0.3 was constant on the whole part of the model. Thus, Young's modulus can be calculated implicitly as a function of depth.

While the north boundary is traction-free, the west, east, and south edges of the domain are subject to roller constraints. 450×225 elements discretize the computational domain at the fine scale with a 22.2 ×13.3 m^2 fine cell size. In order to keep the system in equilibrium at initial reservoir conditions, the initial reservoir pressure is added as a source term for mechanical equilibrium in agreement with $\nabla(C_{dr} : \nabla^s \bar{u} - bpI) = f$, where $f=0$. Ultimately, the reservoir is considered to be fully depleted, thus, the overall pressure drops $p = 100$ bar.

The multiscale solution is obtained with coarsening ratio of 9×9 fine-scale displacement elements per course, resulting in 51×26 coarse displacement nodes against 451×226 nodes on the fine-scale. Fig.3 shows the comparison of the reference fine-scale and multiscale solutions. The error of land subsidence estimation is accessed relative to the fully resolved fine-scale solution as shown in the equation below.

$$\varepsilon = \frac{\left\| x_{ref} - x' \right\|_\infty}{\left\| x_{ref}{}^h \right\|_\infty} = \frac{i \in \{1,2,\ldots,N_h\}^{\left\| x_{ref} - x'_i \right\|}}{i \in \{1,2,\ldots,N_h\}^{\left\| x_{ref}{}^h \right\|}} \qquad (51)$$

For the chosen coarsening ratio, mean error does not exceed 5.3%. Overall, the quality of multiscale solution is satisfactory. This model was totally fit into the model of Skolova et al. and it means that these two models work properly.

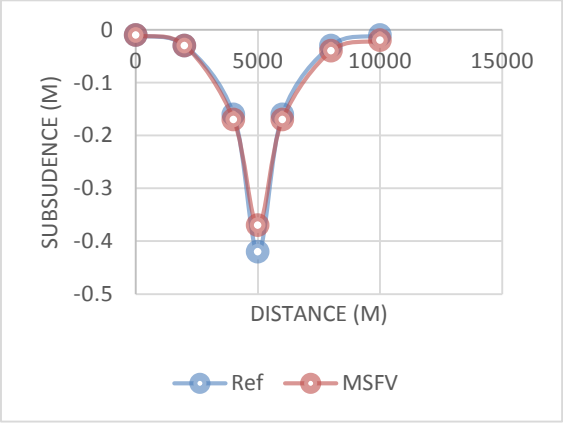

Fig. 3. Comparison of the reference fine-scale (FV) solution in a simple strain subsidence test scenario and the multiscale solution obtained using the EM³GMSR (Enhanced Mixed Multiscale Multiphysics Geomechanical Model with Surrounded Rock) technique (dashed red line) (solid blue line). The fine-scale grid has 450×225 displacement elements compared to the 50 ×25 elements in the coarse-scale mesh of the EM³GMSR.

4. WATER INJECTION IN THE POROUS MEDIUM WITH THE SURROUNDING ROCK LAYERS

The environment around the reservoir will affect its performance. Therefore, in this section, to determine how and to what extent this affects, the problem of injection in a homogeneous deformable porous medium, which was evaluated in Section 4-5, will be re-examined and this time the effect of the surrounding environment will be taken into account, assuming that on the right and left sides of the bounding reservoir, an area ten times the length of the reservoir has been provided to consider its effect on the reshaping of the reservoir. At the top of the reservoir, the height of the rock layers equal to 100 meters has been selected. Figure 4 shows the intended reservoir with the surrounding rock layers. Points A, B, and C are in coordinates (825), respectively. The stiffness of the springs is obtained by applying a single force and dividing it by the deformation obtained in each node. To evaluate how the environment around the reservoir affects, the modulus of elasticity of the rock around the reservoir, 2.5 GPa has been considered. Figure 5 shows the production rate in various non-deformable modes, with deformation without effect of M^{3}GM environment and with deformation with effect of M3GMSR environment with elastic modulus of surrounding rocks.

As can be seen from Figure 5, the harvest rate is much higher regardless of the reservoir deformation, especially at the beginning of the harvest. Higher harvest rates are due to not considering the part of injection energy that is consumed by the deformation of the porous medium. For this reason, after the injection time, it reaches the state of provides equal to other cases. Of course, it should be noted that in both M^{3}GM and M^{3}GMSR models, the relationship of displacement stress is considered linearly elastic. If the stress-strain relationship is considered expensive and plastic based on the properties of the reservoir material, this process will continue until the end of the injection. Because even if the stress remains constant, the reservoir will deform and still part of the energy will be spent on deforming the porous environment and will be consumed. The amount of energy used to deform the solid phase due to the stress-strain curves of the reservoir material will probably be much higher than the elastic value. Also, as shown in Figure 5, the environment around the reservoir will have a significant effect on the harvest rate. In a similar way, the more the environment around the reservoir is firmer and has rocks with a higher modulus of elasticity, the lower the energy consumption and the higher harvest rate. For a more detailed study, three points in reservoir environment, which are shown with the letters A, B, C in Figure 4, are considered. The pressure history at these three points for the various modes is shown in Figure 6. As can be seen from the figure, the pressure at point A, which is closer to the injection site, is further increased. Also, the pressure in other parts of the reservoir is lower than the rigid state in cases of deformation of the porous medium. In fact, considering the deformation of the porous medium, the injection pressure is not completely applied to the fluid and part of it causes the deformation of the solid phase and will be consumed.

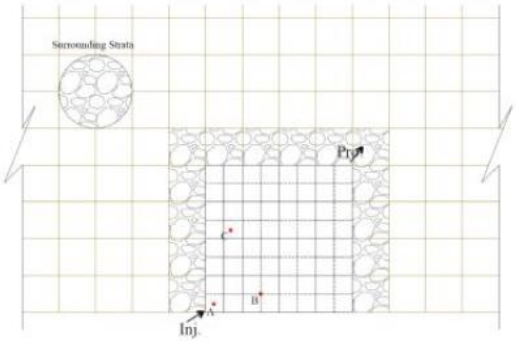

Fig. 4. Reservoir considering the surrounding rock layer.

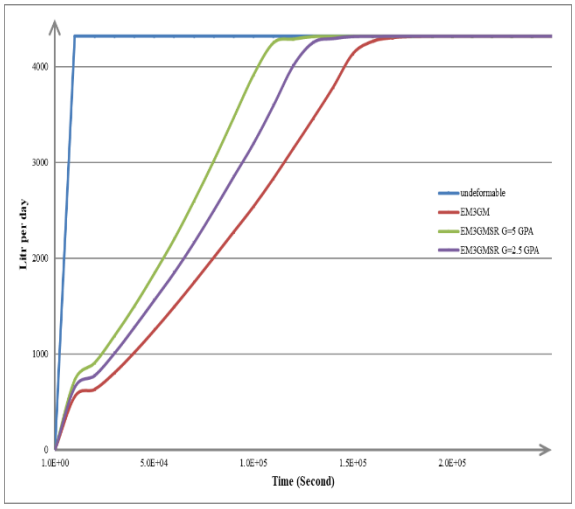

Fig. 5. Reservoir withdrawal rates in different modes.

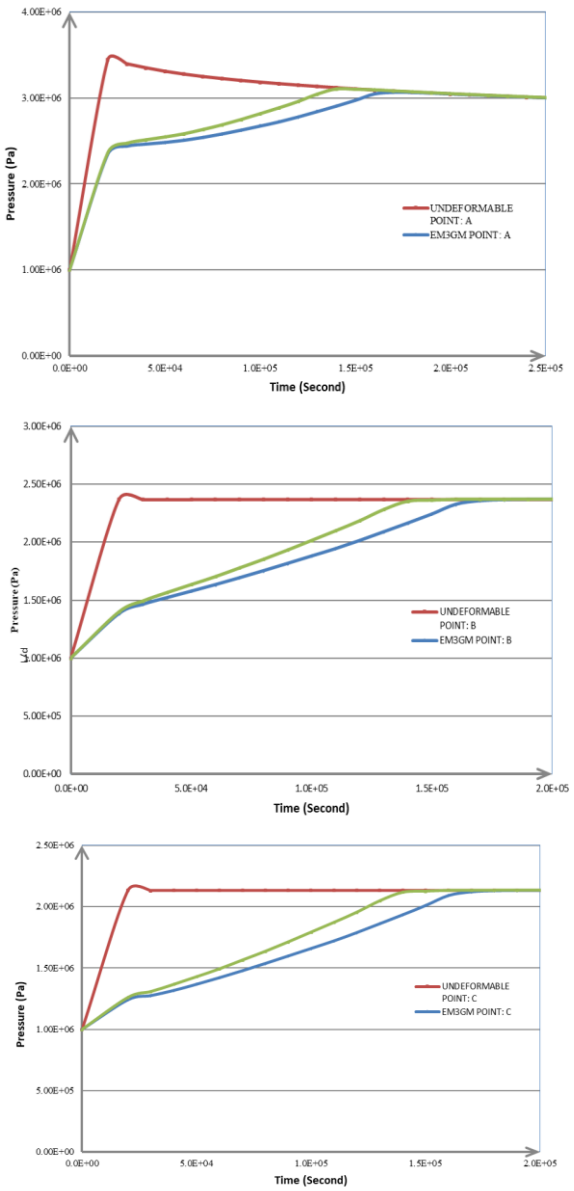

Fig. 6. Pressure history at the point of A, B, and C, respectively.

5. CONCLUSION

The rock deformations in the reservoir play an important role not only for subsidence or heave aspects, but also, with respect to the production rate. In this regard, an Enhanced Mixed Multi-scale, Multi-physical Geomechanical model was advocated in this study. The multiscale finite volume framework for the fluid flow is combined with the finite element for the rock deformation. Considering each phase in the domain of influence has computational privilege. Moreover, plastic deformation through bounding plasticity is also taken into account in order to obtain a better rock behavior prediction. So, in this research:

- Fluids and rocks are simulated through separate frameworks.
- The plastic deformation through bounding plasticity is incorporated.
- The surround rock interaction is simulated with the aid of virtual spring and reasonable agreement with the fine scale simulation is achieved.
- It is observed from the simulation that considering rock plastic deformation will result the lower production rate with respect to more energy loss during plastic deformation.

It is revealed by this research that not only will be decreasing the computational cost by the multiscale modeling, but also, reasonable agreement with the fine scale solution could be verified. It is suggested that the extended finite element could be combined by multiscale framework in order to simulate fault and discontinuity in the fractured rock.

REFERENCES

[1] A Abdollahipour, MF Marji, 2020, A thermo-hydromechanical displacement discontinuity method to model fractures in high-pressure, high-temperature environments, Renewable Energy 153, 1488-1503.

[2] A Abdollahipour, MF Marji, AY Bafghi, J Gholamnejad, 2016, Time-dependent crack propagation in a poroelastic medium using a fully coupled hydromechanical displacement discontinuity method, International Journal of Fracture 199 (1), 71-87.

[3] Abdollahipour A, Fatehi Marji M, Yarahmadi Bafghi AR,Gholamnejad J, 2016, Numerical investigation of effect of crack geometrical parameters on hydraulic fracturing process of hydrocarbon reservoirs, Journal of Mining and Environment 7 (2), 205-214.

[4] Mohaghegh, S., Arefi, R., Ameri, S., Aminiand, K., & Nutter, R. (1996). Petroleum reservoir characterization with the aid of artificial neural networks. Journal of Petroleum Science and Engineering, 16(4), 263-274.

[5] Durlofsky, L. J. (2003, June). Upscaling of geocellular models for reservoir flow simulation: a review of recent progress. In 7th International Forum on Reservoir Simulation Bühl/Baden-Baden, Germany (pp. 23-27).

[6] Warren, J. E., & Price, H. S. (1961). Flow in heterogeneous porous media. Society of Petroleum Engineers Journal, 1(03), 153-169.

[7] Taheri, E. (2013). Multi-scale modeling of oil movement in a deformable porous medium. Ph.D. thesis. Khaje Nasir Toosi University.

[8] Jenny, P., Lee, S. H., & Tchelepi, H. A. (2005). Adaptive multiscale finite-volume method for multiphase flow and transport in porous media. Multiscale Modeling & Simulation, 3(1), 50-64.

[9] Sokolova, I., Bastisya, M. G., & Hajibeygi, H. (2019). Multiscale finite volume method for finite-volume-based simulation of poroelasticity. Journal of Computational Physics, 379, 309-324.

[10] Castelletto, N., Hajibeygi, H., & Tchelepi, H. A. (2017). Multiscale finite-element method for linear elastic geomechanics. Journal of Computational Physics, 331, 337-356.

[11] Ţene, M., Wang, Y., & Hajibeygi, H. (2015). Adaptive algebraic multiscale solver for compressible flow in heterogeneous porous media. Journal of Computational Physics, 300, 679-694.

[12] Cusini, M., Lukyanov, A. A., Natvig, J., & Hajibeygi, H. (2015). Constrained pressure residual multiscale (CPR-MS) method for fully implicit simulation of multiphase flow in porous media. Journal of Computational Physics, 299, 472-486.

[13] Hajibeygi, H., & Tchelepi, H. A. (2014). Compositional multiscale finite-volume formulation. SPE Journal, 19(02), 316-326.

[14] Wang, Y., Hajibeygi, H., & Tchelepi, H. A. (2016). Monotone multiscale finite volume method. Computational Geosciences, 20(3), 509-524.

[15] Sadrnejad, S. A., Ghasemzadeh, H., & Taheri, E. (2014). Multiscale multiphysic mixed geomechanical model in deformable porous media. International Journal for Multiscale Computational Engineering, 12(6).

[16] Taheri, E., Sadrnejad, S. A., & Ghasemzadeh, H. (2015). Multiscale geomechanical model for a deformable oil reservoir with surrounding rock effects. International journal for multiscale computational engineering, 13(6).

[17] Moghadam, S. I., Taheri, E., Ahmadi, M., & Ghoreishian Amiri, S. A. (2022). Unified bounding surface model for monotonic and cyclic behaviour of clay and sand. Acta Geotechnica, 1-17.

[18] Nikadat, N., Fatehi, M., & Abdollahipour, A. (2015). Numerical modelling of stress analysis around rectangular tunnels with large discontinuities (fault) by a hybridized indirect BEM. Journal of Central South University, 22(11), 4291-4299.

[19] Sanaye Pasad, M. (2019). Modeling of oil movement in elastoplastic porous medium by multi-scale method and adaptive networking. Master's thesis. Khaje Nasir Toosi University.

[20] Ghoreishian, S. (2012). Hydraulic-thermal modeling of deformable black oil reservoir s. Ph.D. thesis. Khaje Nasir Toosi University.

[21] Moghadam, S., Taheri, E., & Ahmadi, S. (2018). Modeling soil behavior using an integrated clay-sand model by Euler implicit method. 7th Iran Mining Engineering Conference and 5th Iran International Mining and Mining Industries Congress, Tehran.

[22] Hashiguchi, K., & Chen, Z. P. (1998). Elastoplastic constitutive equation of soils with the subloading surface and the rotational hardening. International Journal for Numerical and Analytical Methods in Geomechanics, 22(3), 197-227.

Appendix: Signs and abbreviations			
definition	**The symbol**	**definition**	**The symbol**
		Relative phase permeability	kr_{α}
The plastic-shaped coefficient in the law of flow	$d\lambda$	Fountains and phase wells	$\dot{\boldsymbol{m}}_{\boldsymbol{\alpha}}$
plastic potential function	Q	Shape function	$\boldsymbol{N}_{\boldsymbol{u}}$
Volumetric strain	ε_v	Area of micro-scale cells	A
Critical mode line slope	M	Phase volumetric formation coefficient	$\boldsymbol{B}_{\boldsymbol{\alpha}}$
Specifies the shape of the yield surface	N	Compressibility coefficient	$\boldsymbol{C}_{\boldsymbol{c}}$
Adjusting the point of collision of the critical mode line with the yield surface	R	Elastic matrix	$\boldsymbol{D}_{\boldsymbol{e}}$
plastic volumetric strain changes	$\boldsymbol{d\varepsilon}_{\boldsymbol{v}}^{\boldsymbol{p}}$	Elasto plastic matrix	$\boldsymbol{D}_{\boldsymbol{ep}}$
Average effective stress	p'	Elastic modulus	E
Convergence range	γ		
Solid phase strain vector	ε	Absolute permeability matrix	$\boldsymbol{K}$
Density of fluid phases	ρ_{α}	Unit vector perpendicular to the surface	$\tilde{\boldsymbol{n}}^{\boldsymbol{h}}$
Matrix of basic functions	Φ_k^h	Fluid Pressure	p
Correction function matrix	Φ^h	unstable microscale pressure	p'
Coarse gride cell vector	Ω_k		
Auxiliary cell vector	Ω^h	Microscale analysis pressure	p_f
Porosity	ϕ	Phase saturation degree	$\boldsymbol{S}_{\boldsymbol{\alpha}}$
Poisson solid phase coefficient	υ	Solid phase deformation vector	$\boldsymbol{u}$
Vector of the weight coefficients of the zone	$\boldsymbol{W}_{\boldsymbol{u}}^{\boldsymbol{t}}$	Fluid phase velocity	$\boldsymbol{v}_{\boldsymbol{\alpha}}$
Vector weight weights of borders	$\tilde{\boldsymbol{W}}_{\boldsymbol{u}}^{\boldsymbol{t}}$	Pastry strain change vector	$d\varepsilon\text{^}p$
Vector of total strain changes	$\boldsymbol{d\varepsilon}$		
Solid phase velocity	$\boldsymbol{v}_{\boldsymbol{s}}$		
Fluid phase mobility matrix	$\boldsymbol{\lambda}_{\alpha}$		